Numerical simulation of electromagnetically driven flow and temperature distribution inside an electric arc furnace with two non-parallel electrodes

M. Herrera-Ortega[a], J. A. Ramos-Banderas[a,*], C. A. Hernández-Bocanegra[a], and A. Beltrán[b]

[a]*Posgrado en Metalurgia, Tecnológico Nacional de México Campus Morelia, Av. Tecnológico No. 1500, Col. Lomas de Santiaguito, 58120, Morelia, Michoacán, México.*

[*]*e-mail: jose.rb@morelia.tecnm.mx*

[b]*Instituto de Investigaciones en Materiales, Unidad Morelia, Universidad Nacional Autónoma de México, Antigua Carretera a Pátzcuaro No. 8701, Col. Ex Hacienda de San José de la Huerta, 58190, Morelia, Michoacán, México.*

Received 08 February 2024; accepted 28 June 2024

In this study, numerical simulations were performed for a three-dimensional computational fluid dynamics model to investigate the flow, thermal, and magnetohydrodynamic behavior inside an electric arc furnace. The simulations consider the interaction of the multiphase flow involving steel, slag, and air, along with the induction of electric current through two non-parallel graphite electrodes. They account for heat transfer resulting from the Joule effect and the impact of the Lorentz force on the fluid dynamics of liquid steel. Experiments using Gaussmeter equipment were conducted during the operation of an electric arc furnace to validate the magnetic flux density generated by the electric current. Results provide comprehensive insights into temperature, velocity, Joule heat, and Lorentz force fields to characterize the flow. The Lorentz force, arising from the interaction between electric current density and magnetic flux density has a maximum value of 164 $\mathrm{N{\cdot}m^{-3}}$, and it was observed to counteract the movement of convective flow induced by buoyancy forces. This counteraction led to a reduction in velocity within the liquid steel of about 4%, consequently resulting in a more uniform temperature distribution throughout the liquid steel with a maximum temperature value significantly lower compared to the case that does not consider the contribution of the Lorentz force.

Keywords: Electric arc furnace; non-parallel electrodes; Joule heating; Lorentz force.

DOI: https://doi.org/10.31349/RevMexFis.71.010603

1. Introduction

Electrical steelmaking is based on using electrical energy to melt, homogenize, and subsequently refine a bath of liquid steel. A key process in electrical steelmaking is the electric arc furnace (EAF), where electrical energy is supplied through high-power transformers via consumable graphite electrodes. In direct current furnaces, the electric arc is generated between the metal bath and the electrodes, while in alternating current furnaces, the electric arc occurs between the electrodes [1]. The electric arc, essential for melting scrap metal, results from the heat generated by the Joule effect. The fluid dynamic behavior is primarily influenced by buoyancy forces arising from high-temperature gradients. Additionally, there is slight agitation due to the Lorentz force generated by the interaction of the electric current with the induced magnetic field.

Globally, steel production through this method constitutes approximately 28% of total production. However, in Mexico, EAF production surpasses 85% of total production [2]. It is crucial to study and comprehend the various mechanisms governing heat transfer, fluid flow, and electromagnetic mixing. These parameters play a vital role in optimizing the process and reducing or preventing failures due to refractory wear. The inherent dangers of high temperatures during the process and the opacity of the furnace materials make impossible the direct observation of the fluid behavior. Consequently, computational fluid dynamics (CFD) has emerged as an effective tool to approximate the solution of governing equations that describe the industrial process. Furthermore, understanding the fluid dynamic behavior is of great help in determining the degree of mixing that can be achieved within the system. The comprehension of mixing rates enables the determination of how ferroalloys dissolve in the bath and traverse the fluid, ultimately achieving chemical homogeneity.

Numerous authors have extensively reported on the numerical simulation of transport phenomena in alternating current arc furnaces utilized in various metal manufacturing processes. Bowman and Edels first investigated the characteristics of alternating current arcs [3]. The authors conducted measurements of the radial temperature distribution in alternating current arc columns for different current values. Their findings revealed that the arc generated with alternating current exhibits a lower temperature and greater power dissipation than arcs generated with direct current. This phenomenon arises from the cyclic radial flow of gas induced by the oscillations of the electric current discharge. Several studies have focused on the temperature distribution and Joule heating aspects in the EAF and similar processes. Yang *et al.* [4] employed a CFD model for a Submerged Arc Furnace (SAF) in Ferrochrome production, revealing a significant temperature gradient beneath the electrodes and near the furnace walls. Additionally, Wang *et al.* [5] proposed a 3D model to estimate electrical energy consumption in MgO

manufacturing, providing insights into the distribution of the thermal field generated by the Joule effect. Kiyoumarsi *et al*. [6] predicted current density, voltage, and magnetic field strength in an EAF. Their findings suggest that axial current density generates an azimuthal induced magnetic field, while radial current density generates an axial induced magnetic field. Mohebi *et al*. [7] developed a two-dimensional model for heat transfer and fluid dynamics in a SAF for ferrosilicon manufacturing. For the time-dependent simulations, they considered the coupling of mass, momentum, and energy equations with Maxwell's equations, evaluating the effects of electric current and arc length on temperature distribution and fluid dynamics. For ferrosilicon production, Scevarsdottir [8] developed a magnetohydrodynamic (MHD) model including radiation and electromagnetic forces. Results show that there is an optimal arc length not greater than 10 cm. This study also compared current density and voltage estimated by the arc channel model (CAM) with in-situ measurements. Kukharev *et al*. [9] proposed a three-dimensional model for the MHD and thermal behavior in a three-phase alternating current furnace. They found that non-uniform heating-induced convection reduces electromagnetic force-generated vortices and induces an additional flow near the furnace walls, improving the mixing in the liquid metal bath. In the same direction, Pavlov [10] studied the interaction between convective flows and electromagnetic force-induced vertical vortices, emphasizing velocity and temperature fields for different electrode configurations and shapes. Later on, different current densities were explored [11]. Yu *et al*. [12] presented a multiphysics model for a SAF, incorporating electromagnetic, fluid flow, and chemical reaction models. The study explored the influence of electrode immersion length on thermal distribution, voltage, and magnetic field, affecting mixing and chemical reactions. In the same direction, Jiang and Zhang [13] developed a multiphysics model describing electromagnetic, thermodynamic, flow, and temperature phenomena in a SAF for MgO production. Karalis [14] proposed different 3D CFD models to analyze operating parameters in EAFs for ferronickel production. These models covered complex phenomena such as charge solidification and fusion and the variation of operational parameters of arc length and current density, electrode thermophysical properties [15], and electrode shape [16,17]. Tesfahunegn *et al*. [18] quantified energy distribution and described the effects of electrode proximity in an alternating current SAF for ferrosilicon production by varying the frequency of the three phases.

In the present study, we performed numerical simulations for a multiphysics model that integrates the electromagnetic phenomenon to analyze the heating induced by the Joule effect in an electric arc furnace featuring two non-parallel electrodes employed for steel scrap melting. This model incorporates a coupled solution, wherein the Lorentz force is considered as a source term in the momentum equation for a multiphase turbulent flow. Owing to the specific arrangement of the electrodes and the furnace geometry, a distinct region is formed, characterized by greater concentrations of heat, magnetic flux density, and current density. This localized concentration plays an important role in determining both the thermal distribution within the furnace and the dynamic fluid behavior of the liquid steel.

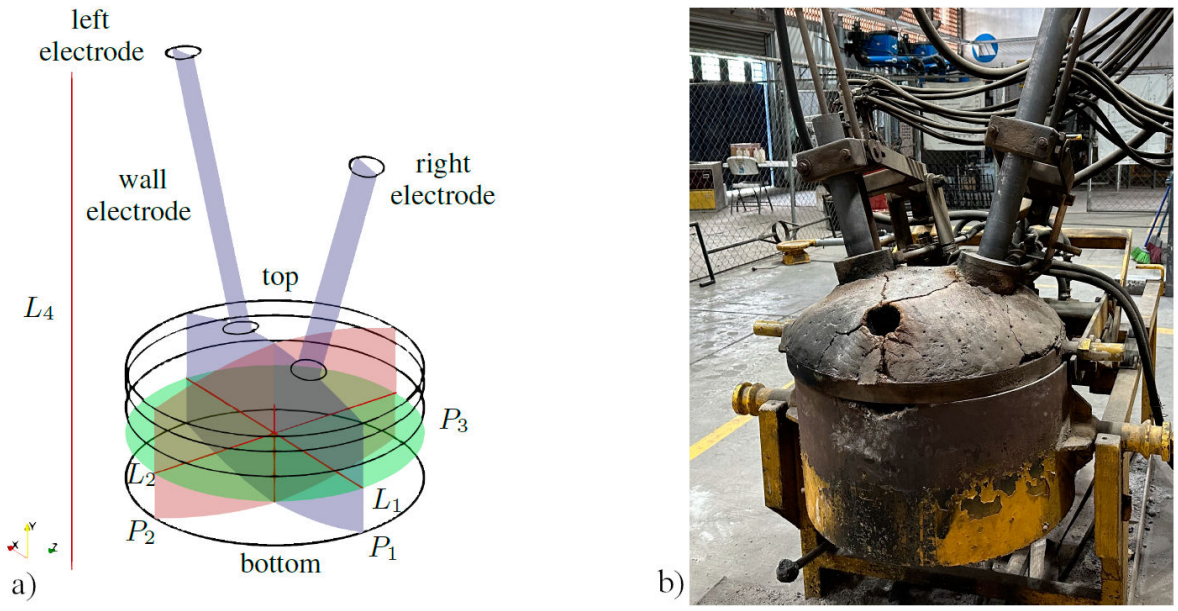

FIGURE 1. Electric arc furnace of 50 kg capacity: a) Computational domain and b) Full scale prototype.

2. Model validation

To validate the numerical simulation of the magnetic field induced by the electric current through the graphite electrodes, measurements of magnetic field density were conducted during the steel scrap melting process in a 50 kg capacity electric arc furnace. The furnace is constructed with a steel sheet shell lined with refractory brick. A sliding dome at the top of the furnace accommodates the two holes through which the graphite electrodes are inserted. The manual electrode leveling system includes a cooling mechanism. The system described above is depicted in Fig. 1, alongside a schematic diagram illustrating the computational domain geometry used in the simulation, with defined zones for the model boundary conditions. Figure 1a) shows the arrangement of planes established for the fluid dynamic, thermal, and electromagnetic analysis. Plane P_1 is located at $z = 0$, plane P_2 is positioned at $x = 0$, and plane P_3 is situated at $y = h/2$. Line L_1 represents the intersection of planes P_1 and P_3, line L_2 is the intersection of planes P_2 and P_3; whereas, line L_3 corresponds to the intersection of planes P_1 and P_2 within the range of $0 < y < 0.18$ m.

The electric current induced through the electrodes varies between 1000 and 3000 A during the whole process due to the manual operation of the furnace. Magnetic field measurements were specifically performed during the flat bath stage, characterized by the complete melting of steel scrap and a more stable electric arc. The electric current during this stage fluctuates between 1000 and 2000 A. A parametric study was conducted to evaluate the influence of variations in current intensity within the furnace's operational range. This study is crucial because the mechanism regulating the arc length is manually activated by an operator, leading to a constant fluctuation in the supplied current intensity throughout the fusion process. It is important to note that the induced current exhibits a lower variation during the flat bath stage as the arc remains more stable. For experimental measurements, a line was established at a distance of 0.45 m from the furnace, extending one meter from the ground. Along this line, 10 measurements were taken at 0.1 m intervals using a transverse Hall effect probe (STD 18-0404) connected to a Gaussmeter (FW Bell 5180). A total of 12 measurements were obtained from four experiments conducted across three melting processes. These experimental measurements were compared against magnetic field density profiles obtained from the numerical simulation along line L_4.

3. Numerical simulation

3.1. Electromagnetic model

Simulations were carried out considering the geometry of the previously described electric arc furnace according to the full-scale prototype dimensions listed in Table I.

First, the electromagnetic fields are solved in a decoupled manner through a finite element method model. In this case

TABLE I. Furnace dimensions.

Parameter	Value (m)
Furnace diameter, d_F	0.25
Electrode diameter, d_E	0.063
Electrode length, l_E	0.8
Steel bath height, h	0.18
Slag layer thickness, h_s	0.02

case the geometry consists of the furnace and two additional volumes. A cartesian domain of 1 m^2 is added to export a uniform grid of data. To capture the source of induced magnetic field and its variation from the center of the physical domain without being affected by the presence of artificial boundaries, a spherical domain that encloses both the furnace and the exported domain is used to simulate an infinite open space surrounding the furnace. For the magnetostatic case the model solves only for the Gauss's magnetic and the Maxwell-Ampére's laws described by Eqs. (1) and (2)

$$\nabla \cdot \mathbf{B} = 0, \tag{1}$$

$$\nabla \times \mathbf{B} = \mu_0 \mathbf{J}, \tag{2}$$

where $\mathbf{B}$ is the magnetic flux density, $\mathbf{J}$ is the current density, and μ_0 is the vacuum permeability. The electric current is defined as an external current density in each of the electrodes to ensure the current flow in a closed loop.

A mesh sensitivity analysis was conducted to confirm the independence of the results concerning the computational mesh density. Results are shown in Fig. 2.

The commercial software COMSOL Multiphysics [19] with the MUMPS algorithm was used for the steady-state solution of the governing equations in a discretized domain with 2.537×10^6 elements.

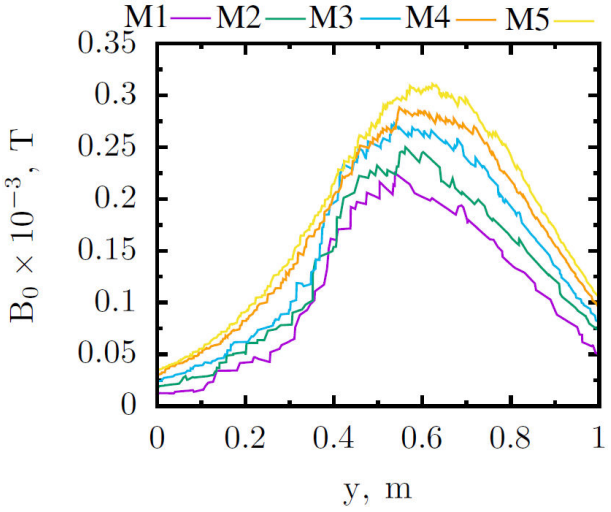

FIGURE 2. Magnetic flux density along L_4 for 5 different discretized domains.

The resultant magnetic field is interpolated across an equidistant grid of points using a C++ routine. This interpolated field is then imported into the ANSYS Fluent MHD module as an external magnetic field.

3.2. MHD model

To perform the coupled simulation of the electromagnetic field along with the energy and momentum equations, the electric scalar potential method was adopted [20-23]. This method effectively couples the simplified Maxwell equations through the ANSYS Fluent interface. The approach involves solving the electric scalar potential equation and calculating the current density employing Ohm's law. The electric field is expressed by Eq. (3)

$$\mathbf{E} = -\nabla\phi - \frac{\partial \mathbf{A}}{\partial t}, \tag{3}$$

where ϕ and $\mathbf{A}$ are the electric scalar potential and the electric vector potential, respectively.

Ohm's law can be described by Eq. (4)

$$\mathbf{J} = \sigma\left(-\nabla\phi + (\mathbf{v}\times\mathbf{B})\right), \tag{4}$$

where the total magnetic field is $\mathbf{B} = \mathbf{b} + \mathbf{B_0}$. $\mathbf{b}$ and $\mathbf{B_0}$ are the induced and externally imposed fields, respectively [24].

Nevertheless, ANSYS Fluent does not support the computation of the induced magnetic field; it solves for an applied external magnetic field. This external field is imported from the simulation conducted in COMSOL. Electric current is applied in the solid domain of the electrodes by entering the domain through the left electrode and leaving the domain through the right electrode ensuring the continuity of electric current density described by (5)

$$\nabla\cdot\mathbf{J} = 0, \tag{5}$$

therefore, the electric scalar potential is given by (6)

$$\nabla^2\phi = \nabla\cdot(\mathbf{v}\times\mathbf{B_0}). \tag{6}$$

For the simulation of the three-phase multiphase flow the volume of fluid model (VOF) is implemented [25]. The VOF can solve for two or more immiscible fluids by tracking the interface between fluids by solving the continuity equation based on the volume fraction of the q phase through Eq. (7)

$$\frac{\partial}{\partial t}(\alpha_q\rho_q) + \nabla\cdot(\alpha_q\rho_q\mathbf{v}_q) = 0, \tag{7}$$

where for the q phase, ρ_q is the density, α_q is the volume fraction inside each cell of the discretized domain occupied by the phase q, and $\mathbf{v}_q$ is the velocity.

The sum of all the q phases is defined through (8)

$$\sum_{q=1}^{n}\alpha_q = 1. \tag{8}$$

The interface lies in cells where the value of the volume fraction is between the interval $0 > \alpha_q > 1$ and is tracked through a geometric reconstruction scheme. Assuming that electric surface current at the interface between phases can be neglected, electrical conductivity for the mixture is given by Eq. (9)

$$\sigma_m = \sum_{q=1}^{n}\sigma_q\alpha_q, \tag{9}$$

where σ_q and α_q are the electric conductivity and the volume fraction of the phase q, respectively. The properties of the mixture such as density, viscosity, etc., are calculated in the same manner.

The momentum equation is solved through the entire domain. The resulting velocity field given by Ec. (10) depends on the volume fraction for all phases through the properties ρ_q and μ_q

$$\frac{\partial}{\partial t}(\rho\mathbf{v}) + \nabla\cdot(\rho\mathbf{v}\mathbf{v}) = -\nabla p + \nabla\cdot\left[\mu\left(\nabla\mathbf{v} + \nabla\mathbf{v}^T\right)\right] + \rho\mathbf{g} + \mathbf{F}, \tag{10}$$

where ρ is the density, μ is the viscosity, ∇p is the pressure gradient, $\mathbf{g}$ is the gravitational acceleration, and $\mathbf{F}$ is the volumetric Lorentz force which is described by Eq. (11) as the product of the interaction between electric current density and magnetic flux density

$$\mathbf{F} = \mathbf{J}\times\mathbf{B}_0. \tag{11}$$

Energy equation is solved for all phases and is described by (12)

$$\frac{\partial}{\partial t}(\rho E) + \nabla\cdot(\mathbf{v}(\rho E + p)) = \nabla\cdot\left(k_{eff}\nabla T + \left(\overline{\overline{\tau}}_{\text{eff}}\cdot\mathbf{v}\right)\right) + \frac{1}{\sigma}\mathbf{J}\cdot\mathbf{J}, \tag{12}$$

where T is temperature and $\overline{\overline{\tau}}_{\text{eff}}$ is the viscous dissipation term. $k_{\text{eff}} = k + k_t$ is the effective conductivity and k_t is the turbulent thermal conductivity, defined according to the turbulence model being used.

The first term on the right-hand side of Eq. (12) represents the energy transfer due to conduction and viscous dissipation; whereas, the second one is for the heat generated by Joule effect. It is added to the energy equation through a volumetric heat source term. $1/\sigma = \rho_{\text{res}} = R\cdot A/L$. R is the electrical resistance of the electrode, and A and L are the cross-section area and length of the electrode, respectively.

The turbulence phenomenon is solved using the two-equation $k-\omega$ model. This approach involves solving the transport equations for turbulent kinetic energy k and the specific dissipation rate ω as described by Eqs. (13) and (14)

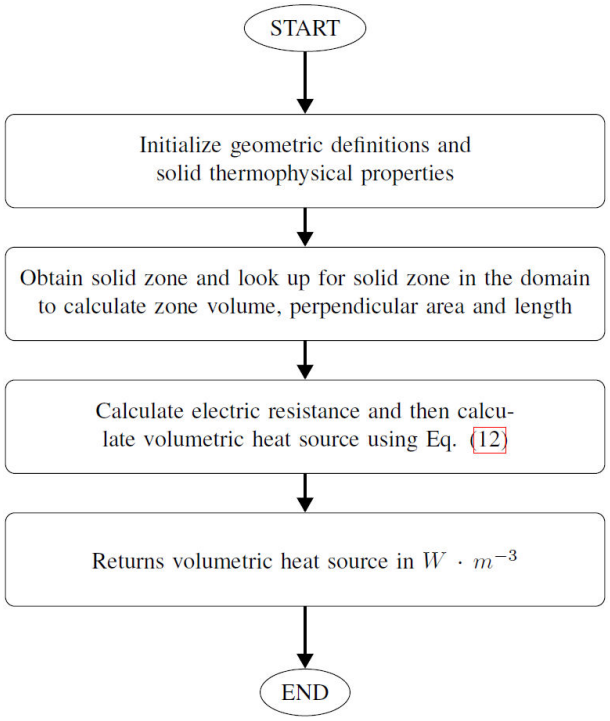

FIGURE 3. Algorithm of volumetric heat source due to Joule effect.

$$\frac{\partial}{\partial}(\rho k) + \frac{\partial}{\partial x_i}(\rho k u_i) = \frac{\partial}{\partial x_j}\left(\Gamma_k \frac{\partial k}{\partial x_j}\right) + G_k - Y_k + S_k + G_b, \quad (13)$$

$$\frac{\partial}{\partial}(\rho \omega) + \frac{\partial}{\partial x_i}(\rho \omega u_i) = \frac{\partial}{\partial x_j}\left(\Gamma_\omega \frac{\partial \omega}{\partial x_j}\right) + G_\omega - Y_\omega + S_\omega + G_{\omega b}, \quad (14)$$

where G_k represents the generation of turbulent kinetic energy due to velocity gradients, G_ω represents the generation of ω. Γ_k y Γ_ω represent effective difussivity of k and ω, respectively. Y_k and Y_ω represent the dissipation of k and ω due to turbulence. S_k and S_ω are source terms and G_b is the source term due to buoyancy forces for both k and ω [6].

The mesh for the MHD model consisted of a discretized domain that includes the fluid confined within the furnace and solid zones representing the two non-parallel electrodes. A mesh sensitivity study was performed, and the final mesh comprised 845,632 elements. The simulation was performed using commercial code ANSYS Fluent in a transient state using the PISO algorithm for the pressure-velocity coupling. The obtained results consider a convergence criterion of 10^{-6} for all equations. For all calculations, the following considerations were taken into account:

- The geometry was made in a 3D cartesian coordinate system.
- Fluids were assumed to be Newtonian.
- A turbulent flow regime was considered.
- The no-slip condition was imposed on all walls.
- Gravity exerted force only along the negative y-axis.
- Surface tension forces between phases were considered.
- The slag was assumed to be sufficiently electrically conductive.
- A closed domain was considered.

The properties of the materials used in the numerical simulation are listed in Table II [16,24,27-29].

To impose a continuous current to the domain, a current volumetric source was added to the solid zones representing the two non-parallel electrodes. To allow the current inflow and outflow, zero current boundaries were set at the top of the electrode volumes. In Table III the boundary conditions (BC) for the different fields are described.

For a comparative analysis, two cases were considered. In case 1, the simulation excludes the impact of electromagnetic forces and only the volumetric heat source was estimated using a User-Defined Function (UDF), as described in the algorithm depicted in the flowchart in Fig. 8, to model the heating due to the Joule effect. In case 2, electromagnetic forces are

TABLE I. Furnace dimensions

Material	Density ($kg \cdot m^{-3}$)	Viscosity ($kg \cdot m^{-1} \cdot s^{-1}$)	Thermal conductivity ($W \cdot m^{-1} \cdot K^{-1}$)	Electrical conductivity ($S \cdot m^{-1}$)	Heat capacity ($J \cdot kg^{-1} \cdot K^{-1}$)	Surface tension ($N \cdot m^{-1}$)
Graphite	1360	-	230	25,000	1800	-
Steel	8586-0.8567T	0.0062	41	710,000	790	-
Slag	3500	0.2662	0.48	100,000	871	-
Air	1.225	1.7894E-05	0.0242	1E-09	1006.43	-
Steel-slag	*	*	*	*	*	1.52
Slag-air	*	*	*	*	*	0.61

*Calculated by Eq. (9)

TABLE III. Boundary conditions for the different variables.

Region/BC	Thermal	Electric potential	Velocity
Left electrode	$\frac{\partial T}{\partial \mathbf{n}} = 0$	4.73×10^5 A/m^2	-
Right electrode	$\frac{\partial T}{\partial \mathbf{n}} = 0$	4.73×10^5 A/m^2	-
Wall electrode	$\frac{\partial T}{\partial \mathbf{n}} = h(T_f - T_s)$	$\frac{\partial \phi}{\partial \mathbf{n}} = 0$	-
Furnace top	$\frac{\partial T}{\partial \mathbf{n}} = \frac{T_1 - T_2}{R_i}$	$\frac{\partial \phi}{\partial \mathbf{n}} = 0$	$\mathbf{v} = 0$
Furnace wall	$\frac{\partial T}{\partial \mathbf{n}} = \frac{T_1 - T_2}{R_i}$	$\frac{\partial \phi}{\partial \mathbf{n}} = 0$	$\mathbf{v} = 0$
Furnace bottom	$\frac{\partial T}{\partial \mathbf{n}} = \frac{T_1 - T_2}{R_i}$	$\frac{\partial \phi}{\partial \mathbf{n}} = 0$	$\mathbf{v} = 0$

considered, and both the heating due to the Joule effect and the Lorentz force are calculated by solving the electric scalar potential formulation using UDF's within the ANSYS Fluent MHD module.

4. Results and discussion

4.1. Magnetic field validation

Measurements were conducted along L_4 using a transverse Hall effect probe connected to a Gaussmeter to validate the magnetic field density. A total of 10 measurements were taken along L_4 with a separation of 0.1 m between each measurement. Across the three fusion processes, four measurements were obtained for each position, resulting in a total of 12 measurements. The results for each position were averaged, and the deviation of the results was estimated to generate the plot in Fig. 4. These experimental results were then compared against magnetic flux density measurements obtained from the simulation on the same line, L_4; as can be seen, the numerical results agree with the experimental ones.

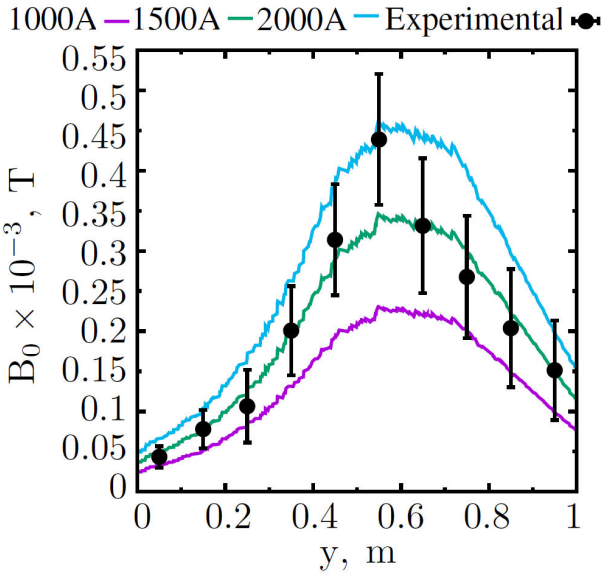

FIGURE 4. Comparison of magnetic flux density obtained through numerical simulation and experimental results obtained during the fusion process.

4.2. Magnetic flux density

External magnetic field contours with streamlines for the three analysis planes obtained from the decoupled electromagnetic simulation are shown in Fig. 5. The external magnetic density is evident outside the electrodes as shown in Fig 5a). Inside the electrode, it exhibits a radial increase due to the skin effect. This phenomenon describes the tendency of an alternating current to distribute itself in a conductor, concentrating current density at the outer surface and diminishing towards the interior of the conductor. Figure 5b) shows a more uniform magnetic flux distribution outside the electrodes. The magnetic flux density is greater closer to the electrodes due to its non-parallel location and uniformly diminishes towards the bottom of the furnace. Additionally, a vortex generated by the induced magnetic field is noticeable near the bottom of the furnace. In Fig. 5c), the magnitude and direction of the magnetic flux density are depicted. The magnetic field displays a solenoidal behavior, indicating that the current density enters the domain through the left electrode and exits the domain through the right electrode in a closed loop. In Fig. 5d), three-dimensional streamlines of the magnetic field generated by the electric current are shown. This visualization further corroborates the solenoidal behavior observed in Fig. 5b) It is evident that the magnetic flux density is higher near the electrodes, gradually diminishing as the streamlines approach the domain walls. Similarly, owing to the imposition of an infinitely long domain, the magnetic field density lines exit the domain without any disturbance from the boundaries.

4.3. Fluid dynamic structure

The convective recirculating pattern is due to the difference in density of steel generated by the high thermal gradient in the vicinity of the electrodes. Steel flows towards the slag layer and then is redirected to the walls where it loses temperature to the exterior of the furnace making the steel flow towards the bottom where it is recirculated again. In Fig. 6 velocity profiles at L_1, L_2, and L_3 are shown. The plots illustrate a decrease in velocity along the x and y-axes, primarily attributed to the Lorentz force generated by the interaction between the magnetic field and electric current. This force

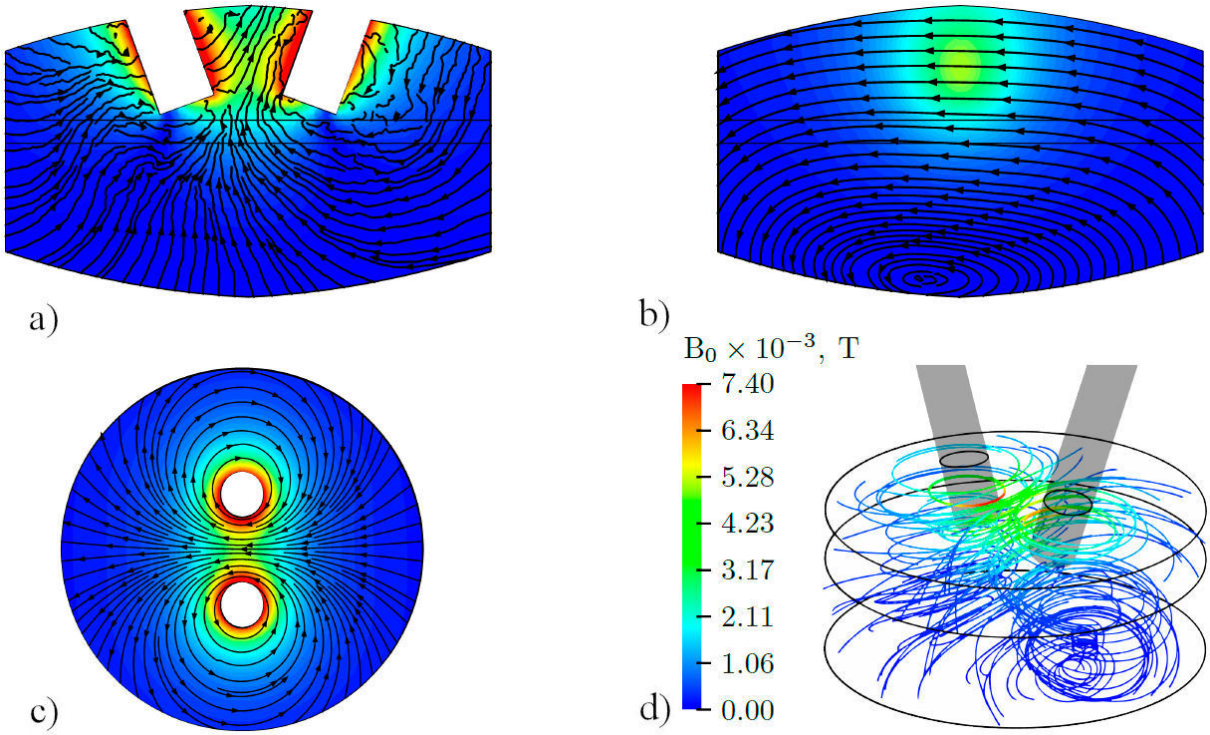

FIGURE 5. Magnetic flux density: a) Plane P_1, b) Plane P_2, c) Plane P_3, d) 3D streamlines.

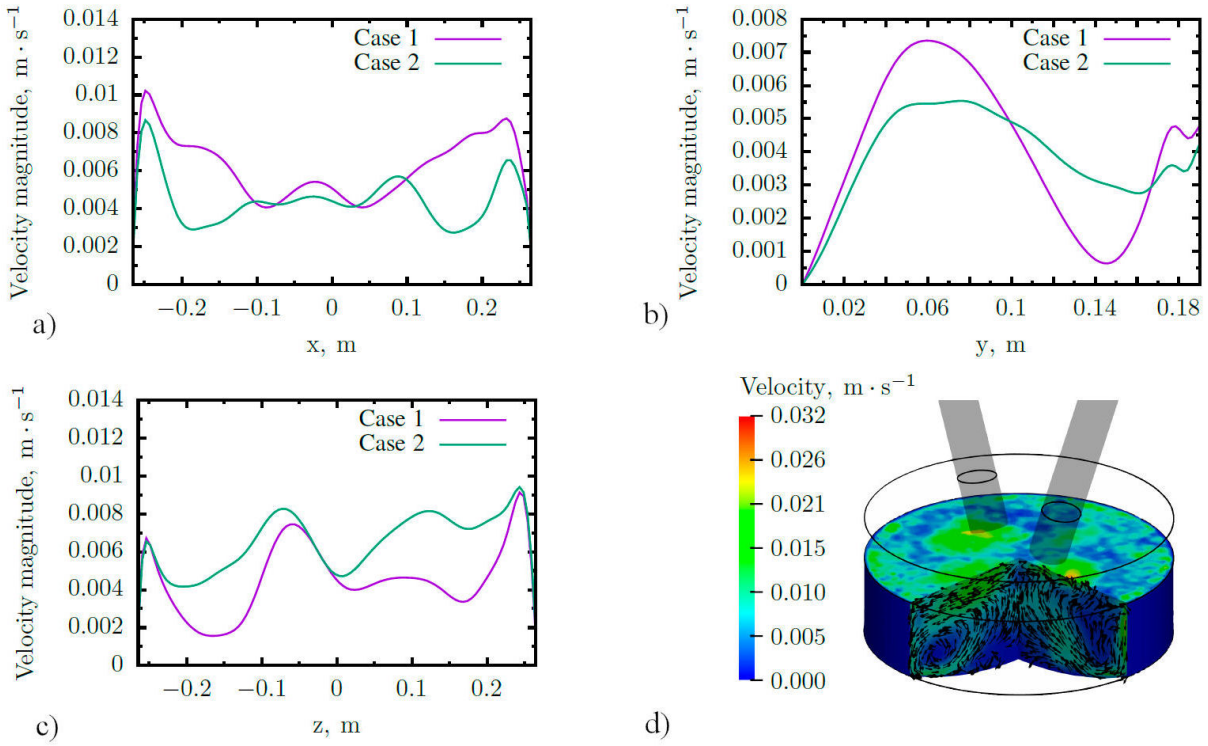

FIGURE 6. Velocity profiles: a) Line L_1, b) Line L_3, c) Line L_2 and d) Contours and velocity vectors. Color bar is the magnitude of the velocity.

opposes the convective flow generated by buoyancy forces. However, in the velocity profile along the z-axis, a slightly higher velocity for Case 2 is observed, although it follows a similar structural behavior to Case 1. In Fig. 6a) and 6c), it is evident that for both cases, the maximum velocity values are located near the walls, gradually decreasing as it approaches

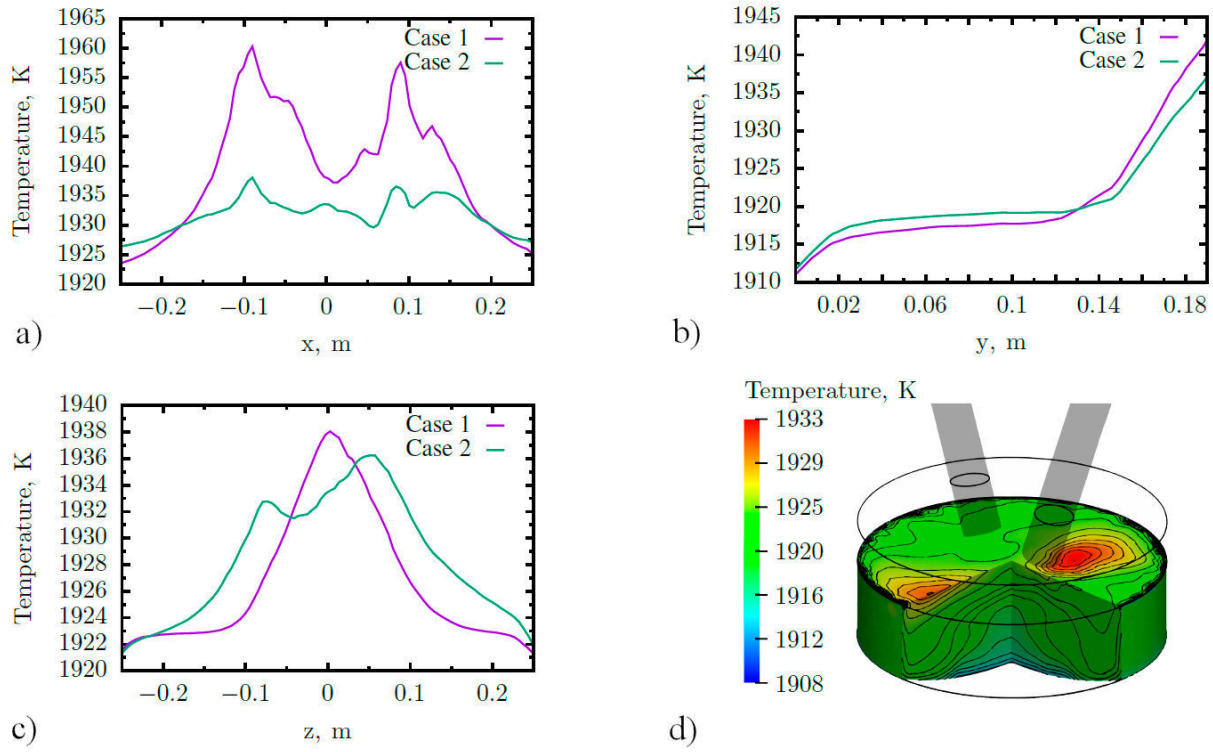

FIGURE 7. Temperature profiles: a) Line L_1, b) Line L_3, c) Line L_2 and d) Temperature contours.

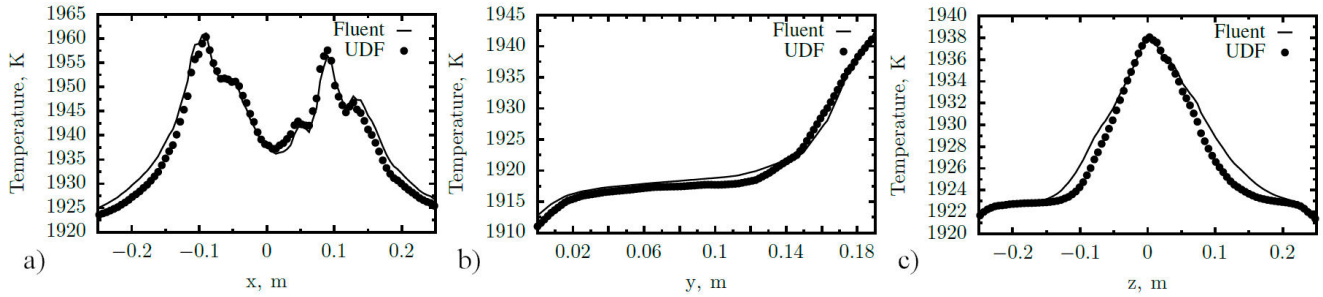

FIGURE 8. Comparison of temperature profiles along different lines calculated through the ANSYS Fluent MHD module and the user-defined function (UDF).

the center of the domain. Conversely, Fig. 6b) displays an increase in velocity for case 1 as it approaches the electrode area, where temperature rises due to heating by the Joule effect. For case 2, the intensity of the magnetic field and current density is greater in the electrode area, implying an increase in the Lorentz force that counteracts the convective flow induced by thermal stratification. This generates a deceleration of the liquid steel moving towards the free surface of the furnace. Fig. 6d) shows the velocity contours and velocity vectors clipped in planes P_1 and P_2. The maximum value of velocity for Case 1 is 8.74×10^{-2} m·s^{-1} whereas for Case 2 it is slightly higher with a value of 9.10×10^{-2} m·s^{-1}.

4.4. Thermal distribution

Figure 7 compares temperature profiles between case 1 and case 2. In Fig. 7a), a decrease in the maximum temperature value is evident. For Case 1, the temperature profile clearly depicts an increase generated by the two heat sources and a decrease in temperature in areas close to the walls where the furnace loses heat to the environment. In contrast, for Case 2, a lower but more homogeneous temperature is observed along L_1. In Fig. 7b), a similar behavior is observed for both cases, with a slight decrease in temperature for case 2 in the area close to the electrodes. Figure 7c) displays the temperature profile over L_2. For case 1, there is an increase in the midpoint of L_2, the line crossing the domain between the two electrodes, indicating an expected higher temperature due to its proximity to the electrodes. In contrast, for case 2, a decrease in temperature is noted, but with a more uniform temperature distribution along L_2. The temperature distribution changes are partially due to the increase in velocity caused by the Lorentz force in case 2. This helps to explain the displacement of the hot spots in case 1, which are located below

the electrodes as shown in Fig. 7a). The electromagnetically generated motion improves the heat transfer by convection, decreasing the temperature and promoting a more homogeneous temperature distribution, as observed along lines L_1 and L_2.

Figure 8 presents a comparative analysis between the Joule heat formulation calculated using the Magnetohydrodynamics (MHD) module and the user-defined function (UDF) for establishing a volumetric heat source in case 1, which excludes the effect of electromagnetic forces. The comparison focuses on the thermal stratification generated by the supply of electrical energy through the electrodes. The plots demonstrate that the UDF accurately calculates the thermal contribution of the electrodes to the liquid steel bath.

The UDF for the heat source proves to be highly advantageous in cases where only heating by the Joule effect is considered, omitting the effects of electromagnetic forces. This can significantly reduce calculation time by passing the solution of the MHD formulation. However, the contribution of the Lorentz force to the fluid dynamic pattern can significantly affect the thermal distribution of the liquid metal bath as seen in Fig. 9, and by using the UDF it is omitting the computation of the source term in the momentum equation.

The maximum value of temperature for Case 1 is 1995 K whereas for Case 2 the maximum temperature is significantly lower with a value of 1945.57 K which is a difference of almost 50 K. The plots in Fig. 10 illustrate the heat generated by the Joule effect, estimated using the Fluent MHD module.

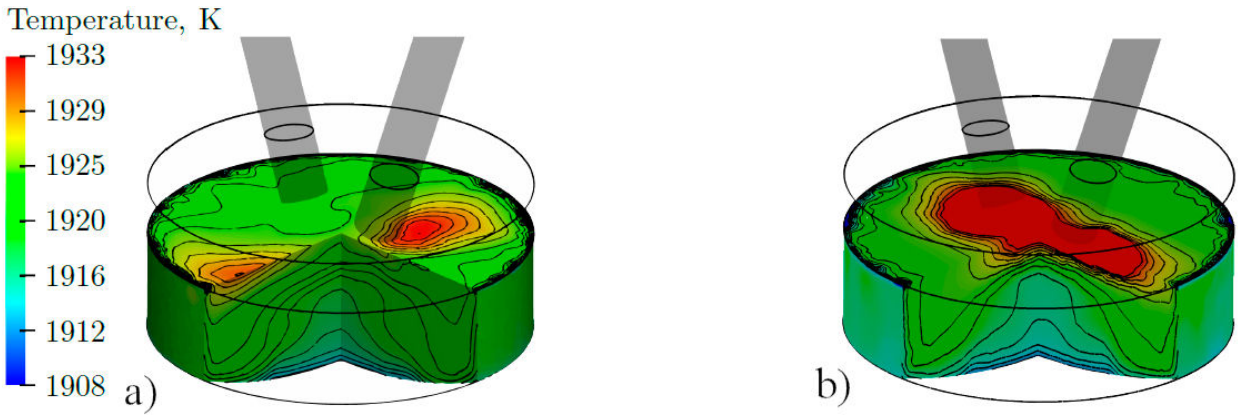

FIGURE 9. Comparison of thermal distribution of liquid steel bath: a) Case 1 using UDF and b) Case 2 using MHD module and taking into account the Lorentz force contribution to the momentum equation.

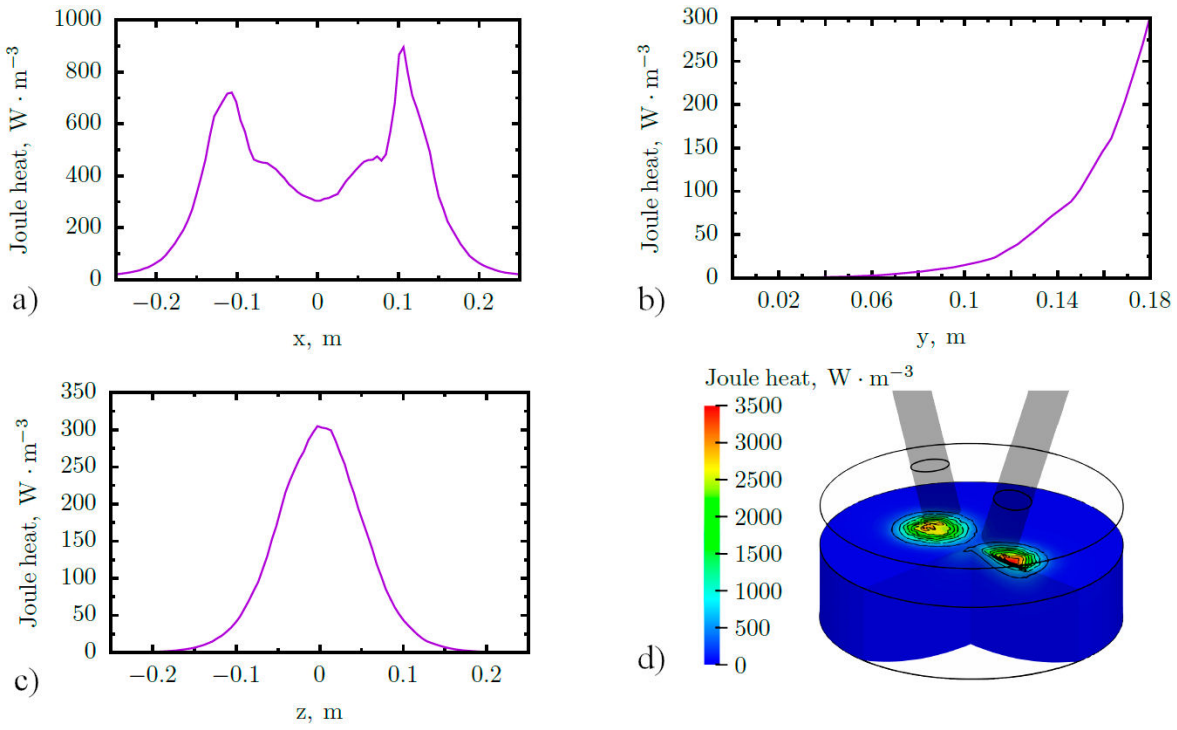

FIGURE 10. Joule heat profiles: a) Line L_1, b) Line L_3, c) Line L_2 and d) Joule heat contours.

In Fig. 10a), it is evident that along L_1, there is an increase in the areas close to the two electrodes, mirroring the temperature profiles. For L_3, as depicted in Fig. 10b), there is an increase in heat due to the Joule effect on the symmetry axis, with a value of practically 0 at the bottom of the furnace and a maximum value in the area where the electrodes are immersed into the slag and closer to the liquid steel bath. Finally, Fig. 10c) shows the heat distribution due to the Joule effect along L_2, indicating an increase in the area close to the electrodes.

5. Conclusions

A comprehensive multiphysics numerical model was developed, incorporating the influence of electromagnetic forces within a conductive fluid in a stratified multiphase flow. This model accounts for the heat generated by the Joule effect resulting from the induction of electric current through non-parallel graphite electrodes in an alternating current electric arc furnace. Employing a stationary numerical approach that solves Gauss's magnetic law and the Maxwell-Ampere law to describe the magnetic field induced by the electric current, the magnetic field density was obtained. Subsequently, this magnetic field density was introduced into the ANSYS Fluent Magnetohydrodynamics (MHD) module to investigate the impact of electromagnetic forces on an electric arc furnace. The conclusions from this study are as follows:

1. The fluid dynamic structure within the furnace is governed by the effect of buoyancy forces due to the difference in density in the liquid steel caused by the temperature gradients induced by the graphite electrodes which are the volumetric source of heat by Joule effect.

2. The Lorentz force generated by the interaction of electric current density and magnetic flux density opposes the movement of convective currents produced by buoyancy forces. This causes a decrease in velocity within the liquid steel in the zones near the walls but velocity increases in the zone near the electrodes due to the Lorentz force produced which in turn causes a more homogeneous temperature distribution within the liquid steel.

3. Although the Lorentz force contributes to a lesser extent compared to the buoyancy forces, not including electromagnetic forces in the simulation can lead to an overestimation of the maximum temperature inside the furnace by almost 50 K, although a temperature measurement of the liquid steel inside the furnace is required to validate this statement.

4. For the case in which electromagnetic forces are not included in the simulation, the UDF satisfactorily solves the heat contribution due to the Joule effect through a volumetric heat source in the solid domain of the electrodes; however, the maximum temperature inside the steel domain increases by almost 3%.

5. The numerical simulation of the magnetic flux density was successfully validated by magnetic field density measurements carried out during the operation of the electric arc furnace in a melting process.

6. There is an increase in both turbulent kinetic energy and the specific dissipation rate of around 14% for both quantities by taking into account the electromagnetic forces in the fluid dynamics analysis. This suggests an increase in the chaotic motion of liquid steel, which can explain the thermal distribution being more uniform. On the other hand, the increase in the specific dissipation rate suggests that turbulence is being dissipated more rapidly into heat through viscous effects.

Acknowledgments

This research was made possible through the generous support of CONAHCyT via the national scholarship program. The authors want to acknowledge TecNM Campus Morelia, IIM-UNAM Campus Morelia, CONAHCyT and SNI for the permanent support to the academic group of Modeling of Metallurgical Processes. Alberto Beltrán also acknowledges financial support from the CONAHCyT CF-2023-I-1373 and UNAM-DGAPA-PAPIIT IN107722 projects.

1. D. Mazumdar and J. W. Evans, Modeling of steelmaking processes (CRC press, 2009), pp. 8-10.

2. World Steel Association, Steel Statistical Yearbook, Disponible en línea: https://www. worldsteel.org/steel-by-topic/statistics/ World-Steel-in-Figures.html (2022),

3. B. Bowman and H. Edels, Radial temperature measurements of alternating current arcs, *Journal of Physics D: Applied Physics* **2** (1969) 53, https://doi.org/10.1088/0022-3727/2/1/309.

4. Y. Yang, Y. Xiao, and M. Reuter, Analysis of transport phenomena in submerged arc furnace for ferrochrome production, In International Ferroalloy Congress, *SAIMM* (2004) 15-25.

5. Z. Wang, N. Wang, and T. Li, Analysis of power consumption in a submerged arc furnace for MgO single crystal production, In 2010 International Conference on Electrical and Control Engineering (IEEE, 2010) pp. 433-436, https://doi.org/10.1109/iCECE.2010.112.

6. A. Kiyoumarsi *et al.*, Three dimensional analysis of an AC electric arc furnace, In 2009 35th Annual Conference of IEEE Industrial Electronics (IEEE, 2009) pp. 3697-3702, https:

//doi.org/10.1109/iCECE.2010.112.

7. M. M. Moghadam, S. Seyedein, and M. R. Aboutalebi, Fluid flow and heat transfer modeling of AC arc in ferrosilicon submerged arc furnace, *Journal of iron and steel research, international* **17** (2010) 14, https://doi.org/10.1016/S1006-706X(10)60135-5.
8. G. Saevarsdottir *et al*., High-power AC arcs in metallurgical furnaces, High Temperature Material Processes: *An International Quarterly of High-Technology Plasma Processes* **5** (2001), https://doi.org/10.1615/HighTempMatProc.v5.i1.20.
9. A. Kukharev *et al.*, The peculiarities of convective heat transfer in melt of a multiple-electrode arc furnace, *Metals* **9** (2019) 1174, https://doi.org/10.3390/met9111174.
10. S. Pavlovs *et al.*, Numerical Modelling of Melt Circulation in Industrial-size Furnaces with Power Supply by Inductor and over Electrodes, In International Scientific Colloquium Modelling for Electromagnetic Processing pp. 363-369.
11. S. Pavlovs, A. Jakovi'cs, and A. Chudnovsky, Electrovortex flow and melt homogenization in the industrial direct current electrical arc furnace, *Magnetohydrodynamics* (0024-998X) **58** (2022), https://doi.org/0.22364/mhd.58.3.7.
12. Y. Yu *et al*., Modeling on reduction reaction of metal oxides for submerged arc furnace in ferrochrome pellets smelting process, *Metallurgical and Materials Transactions B* **52** (2021) 3907, https://doi.org/10.1007/s11663-021-02304-5.
13. T. Jiang and W. Zhang, Numerical Simulation of Multi-Physics Fields in Fused Magnesia Furnace, *Metals* **13** (2022) 39, https://doi.org/10.3390/met13010039.
14. K. Karalis *et al*., Computational fluid dynamics analysis of a three-dimensional electric submerged arc furnaceoperation (2020)
15. K. Karalis *et al*., Pragmatic analysis of the electric submerged arc furnace continuum, *Royal Society Open Science* **4** (2017) 170313, https://dx.doi.org/10.1098/rsos.170313.
16. K. Karalis *et al.*, Electromagnetic phenomena in an electric submerged arc furnace, In METAL 2015-24th International Conference on Metallurgy and Materials, *Conference Proceedings* (2015) pp. 60-66.
17. K. Karalis *et al*., A CFD analysis of slag properties, electrode shape and immersion depth effects on electric submerged arc furnace heating in ferronickel processing, *Applied Mathematical Modelling* **40** (2016) 9052, https://dx.doi.org/10.1016/j.apm.2016.05.045.
18. Y. A. Tesfahunegn *et al*., The effect of frequency on current distributions inside submerged arc furnace, In 2018 IEEE MTT-S International Conference on Numerical Electromagnetic and Multiphysics Modeling and Optimization (NEMO) (IEEE, 2018) pp. 1-4, https://doi.org/10.1109/NEMO.2018.8503083.
19. COMSOL Inc., COMSOL Multiphysics reference manual (2020), URL https://www.comsol.com/..
20. S. Smolentsev, S. Cuevas, and A. BeltrÃ¡n, Induced electric current-based formulation in computations of low magnetic Reynolds number magnetohydrodynamic flows, *Journal of Computational Physics* **229** (2010) 1558, https://doi.org/10.1016/j.jcp.2009.10.044.
21. A. Beltrán, MHD Natural convection flow in a liquid metal electrode, A*pplied Thermal Engineering* **114** (2017) 1203 , https://doi.org/10.1016/j.applthermaleng.2016.09.006.
22. T. Aguilar-García *et al*., Effect of electromagnetically driven liquid metal flows on the electric potential difference in a cuboid vessel, *Journal of Power Sources* **483** (2021) 229162, https://doi.org/10.1016/j.jpowsour.2020.229162.
23. K. Acosta-Zamora and A. Beltrán, Study of electromagnetically driven flows of electrolytes in a cylindrical vessel: Effect of electrical conductivity, magnetic field, and electric current, *International Journal of Heat and Mass Transfer* **191** (2022) 122854, https://doi.org/10.1016/j.ijheatmasstransfer.2022.122854.
24. P. A. Davidson and A. Thess, Magnetohydrodynamics, vol. 418 (Springer Science & Business Media, 2002).
25. C. W. Hirt and B. D. Nichols, Volume of fluid (VOF) method for the dynamics of free boundaries, *Journal of computational physics* **39** (1981) 201, https://doi.org/10.1016/0021-9991(81)90145-5.
26. F. R. Menter, Improved two-equation k-omega turbulence models for aerodynamic flows, Tech. rep. (1992).
27. R. Rafiei, A. Kermanpur, and F. Ashrafizadeh, Numerical thermal simulation of graphite electrode in EAF during normal operation, *Ironmaking & Steelmaking* **35** (2008) 465.
28. A. W. Cramb and I. Jimbo, Calculation of the interfacial properties of liquid steel-slag systems, *Steel research* **60** (1989) 157.
29. L. Jonsson and P. Jönsson, Modeling of fluid flow conditions around the slag/metal interface in a gas-stirred ladle, *ISIJ Int.* **36** (1996) 1127.